IS-T 1871

Microstructural Characterization of a Zr-Ti-Ni-Mn-V-Cr Based AB*2*-Type Battery Alloy

by

Shi, Zhan

MS Thesis submitted to Iowa State University

Ames Laboratory, U.S. DOE
Iowa State University
Ames, Iowa 50011

Date 1999

PREPARED FOR THE U.S. DEPARTMENT OF ENERGY
UNDER CONTRACT NO. W-7405-Eng-82.

DISCLAIMER

This report was prepared as an account of work sponsored by an agency of the United States Government. Neither the United States Government nor any agency thereof, nor any of their employees, makes any warranty, express or implied, or assumes any legal liability or responsibility for the accuracy, completeness or usefulness of any information, apparatus, product, or process disclosed, or represents that its use would not infringe privately owned rights. Reference herein to any specific commercial product, process, or service by trade name, trademark, manufacturer, or otherwise, does not necessarily constitute or imply its endorsement, recommendation, or favoring by the United States Government or any agency thereof. The views and opinions of authors expressed herein do not necessarily state or reflect those of the United States Government or any agency thereof.

This report has been reproduced directly from the best available copy.

AVAILABILITY:

To DOE and DOE contractors: Office of Scientific and Technical Information
P.O. Box 62
Oak Ridge, TN 37831

prices available from: (615) 576-8401
FTS: 626-8401

To the public: National Technical Information Service
U.S. Department of Commerce
5285 Port Royal Road
Springfield, VA 22161

TABLE OF CONTENTS

ABSTRACT

Transmission Electron Microscopy (TEM), combined with X-ray Diffraction (XRD) and Scanning Electron Microscopy (SEM) was employed to investigate a proprietary and multicomponent AB_2 type Nickel-Metal Hydride (Ni-MH) battery alloy. This material was prepared by High Pressure Gas Atomization (HPGA) and examined in both the as-atomized and heat treated condition. TEM examination showed a heavily faulted dendritic growth structure in as-atomized powder. Selected Area Diffraction (SAD) showed that this region consisted of both a cubic C15 structure with lattice constant a=7.03 and an hexagonal C14 structure with lattice parameter a=4.97Å, c=8.11Å. The Orientation Relationship (OR) between the C14 and C15 structures was determined to be $(111)[1\bar{1}0]_{C15} // (0001)[11\bar{2}0]_{C14}$. An interdendritic phase possessing the C14 structure was also seen. There was also a very fine grain region consisting of the C14 structure. Upon heat treatment, the faulted structure became more defined and appeared as intercalation layers within the grains. Spherical particles rich in Zr and Ni appeared scattered at the grain boundries instead of the C14 interdendritic phase. The polycrystalline region also changed to a mixture of C14 and C15 structures. These results as well as phase stability of the C15 and C14 structures based on a consideration of atomic size factor and the average electron concentration are discussed.

INTRODUCTION

General Background

Hydrogen is an ideal fuel choice because it is a clean, abundant, endless source of energy. When it burns it produces only water, which can be broken down to hydrogen and oxygen, and it has an extremely high gravimetric specific energy. However, using hydrogen as a fuel poses several problems. The gaseous nature of hydrogen requires large storage volumes unless it is compressed. Compressed hydrogen is a significant safety hazard and storage cylinders are bulky and impractical for many applications. To be used in the liquid form, hydrogen would have to be maintained at 20 degrees above the absolute zero, requiring expensive cryogenic equipment. Therefore, the safest and most practical method of employing hydrogen as a fuel source is in rechargeable batteries. It is for this reason that the nickel metal hydride (Ni-MH) rechargeable batteries have gained so much recognition and have been developed rapidly in the last decade. They offer the promise of a safe, rechargeble source of energy. Another driving force for their development is that Ni-MH batteries may be used to replace environmentally hazardous Nickel-Cadium batteries. Other appreciable advantages of Ni-MH batteries include: much higher energy density than Ni-Cd batteries; high discharge current; good cycle life and the capability to be completely recycled.

The essential difference between Ni-MH and Ni-Cd batteries is the difference in the negative electrode rather than a structural difference. It is known that hydrogen is absorbed dissociatively by metallic crystalline surfaces of some types of metals and alloys, with a typical hydrogen to metal ratio of one [1, 2]. These types of metals and alloys form unstable hydrides either exothermically or endothermically [3]. The hydrides are capable of absorbing large amounts of hydrogen in the solid crystalline state. When heated the hydride phase releases (or discharges) hydrogen and gains hydrogen (recharges) again when cooled in a reversible process. Such metal alloys can be utilized as the negative electrode in the Ni-MH battery where M is the appropriate metal or alloy. The Ni-MH battery that has such a negative electrode is able to absorb hydrogen reversibly. A schematic [4] of the charging (dashed arrows) and discharging (arrows) reactions of a Ni-MH battery is shown in Figure 1.

When a rechargeable Ni-MH battery goes through the charging process, hydrogen ions from the electrolyzed water present in the battery are reduced and turn into hydrogen. The hydrogen, in turn, is absorbed by the metal-hydride cathode. When the process is reversed, the hydrogen oxidizes and reunites with oxygen, forming water and producing molecular hydrogen [5].

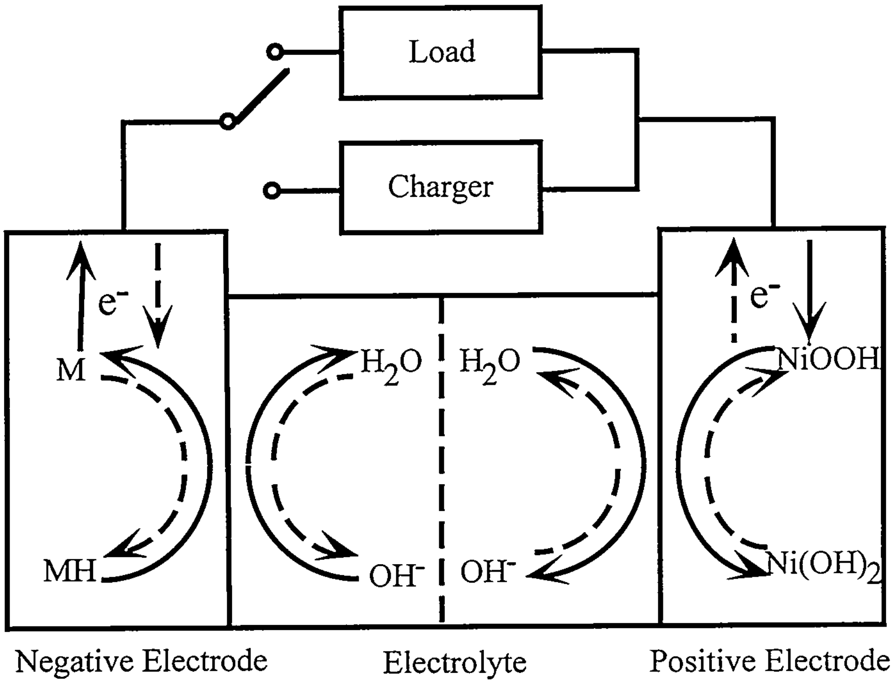

Figure 1. Schematic of the charging (dashed arrows) and discharging reactions of a Ni-MH battery.

The charging and discharging reactions of a Ni-MH battery electrode in alkaline electrolytes can be written as [6]:

$$\text{i. } M + H_2O + e^- \underset{\text{discharge}}{\overset{\text{charge}}{\rightleftarrows}} M - H_{ads} + OH_{int}^-$$

$$\text{ii. } M - H_{ads} \underset{\text{discharge}}{\overset{\text{charge}}{\rightleftarrows}} M\underline{H} \qquad OH_{int}^- \longrightarrow OH_{bulk}^-$$

$$\text{iii. } M\underline{H} \underset{\text{discharge}}{\overset{\text{charge}}{\rightleftarrows}} MH \qquad 2H_{ads} \longrightarrow H_2$$

In these equations, M is the hydrogen storage alloy, $M - H_{abs}$ denotes the hydrogen on the surface of the alloy, $M\underline{H}$ represents the hydrogen in the bulk of alloy and the MH refers to the condensed hydride phase. The first stage is the charge-transfer. In this reaction, the absorbed hydrogen and hydroxide ions are formed at the electrode-electrolyte interfaces. The second stage is hydrogen dissolution and the diffusion of the absorbed hydrogen in the bulk alloy while the hydroxide ions diffuse into the bulk of the electrolyte. The third stage is the condensed phase recrystallization. The hydrogen stores in the metallic lattice in the form of a hydride. In the case of MH electrode overcharge, the hydrogen will be evolved as gas. In the process of discharging, hydrogen stored in the bulk alloy is brought to the electrode-electrolyte interfaces where it is oxidized. The complete electrode reaction can be expressed as:

$$M + H_2O + e^- \underset{\text{discharge}}{\overset{\text{charge}}{\rightleftarrows}} MH + OH^-.$$

Historical Review

The first investigations into using binary and pseudo-binary metal hydride alloys reversibly as hydrogen absorbing sources for use in electrochemical cells appeared in the early 1970s [7]. Since then investigations concerning these alloys have been conducted primarily at Brookhaven National Laboratory in New York [8] and Philips Research Laboratory in Eindhoven, the Netherlands [9]. Table 1 shows the history of hydrogen storage material and Ni-MH battery research [10]. Three types of compounds of multi-component alloys have been successfully used for Ni-MH electrode manufacture [5,6,7]:

- the AB_5 (the prototype alloy is $LaNi_5$);
- the AB_2 (the prototype alloy is ZrV_2);
- the AB/A_2B (the prototype alloy is $TiNi/Ti_2Ni$).

Table 1. The development of hydrogen storage materials and Ni-MH batteries [9].

Time	Development/Introduction
1970	MH electrode of $TiNi$-Ti_2Ni alloy
1970	MH electrode of $LaNi_5$
1978	MH electrode of $LaNi_{5-x}M_x$ alloy, Battery of $LaNi_5$ alloy
1984	$LaNi_{2.5}Co_{2.5}$ base for multiple element alloy
1985-1990	Mixed rare-earth base alloy, hydrogen storage alloy produced mainly by surface-treating technology of high capacity alloys for Ni-MH battery
1991-present	Large scale production of Ni-MH batteries

Among hydrogen storage alloys, AB_5 type alloys are commercially more favored and better developed as negative electrode materials than others. In the past 25 years, it seems that every battery company around the world has tried to developed the Ni-MH battery by utilizing excusively the $LaNi_5$ type of alloy [11]. High capacity Ni-MH batteries which utilize the AB_5 type alloys were commercialized in 1996. The volumetric energy density of these batteries are higher than Li ion batteries.

The Ovonic Battery Company (OBC), as a subsidiary to Energy Conversion Devices, has been intensively involved in pioneer work on the AB_2 type alloy and developing nickel-metal hydride batteries. Their AB_2 type Ni-MH batteries have emerged as the leading battery technology for electric vehicle applications [12]. The AB_2 type Ovonics alloys are multiphase, each phase absorbing large amounts of hydrogen, and claimed to have catalytic activity [13]. Compositional and structural disorders in this alloy are claimed to allow higher hydrogen storage and better kinetics than in conventional MH alloys.

Manufacture Methods

Ni-MH alloys are presently being commercialized and developed for a variety of applications. In most cases, these alloys were prepared by the following steps 1) arc-melting of the constituents in appropriate proportions in an inert gas atmosphere or chill casting of large ingots weighting several hundreds pounds; 2) extensive heat treatment of the ingots (typically it takes days in a controlled inert atmosphere furnace) to eliminate the microscopic compositional inhomogeneity that results during the solidification process, and to promote grain growth and crystalline perfection; and 3) grinding of the annealed ingots into fine powders to produce the high surface area suitable for rapid electrochemical reaction.

In some cases mechanical alloying and annealing techniques [14,15,16] have also been used to produce these alloys. Another method involves the single reaction of hydrogen absorption/desorption, a hydride-dehydride (HDH) process, to fracture large ingots into smaller pieces resulting in a product with an average grain diameter of 200 microns [17,18].

The chemical homogeneity of the alloy is of special concern. Segregation occurs inevitably in the ingot during cooling in the conventional method. Rapid solidification of hydrogen storage alloys has been developed to minimize the effect of segregation. High Pressure Gas Atomization (HPGA) is being investigated as a way to not only minimize the effect of segregation but also reduce processing costs of the AB_2 compound.

In HPGA, a stream of molten materials is blasted with extremely cold Argon or Helium gas at up to three times the speed of sound. The process converts the materials into fine liquid particles which solidify quickly and are nearly spherical in shape. Due to the rapid solidification, the particles have virtually identical chemical compositions. The homogeneity of the HPGA powder is a key advantage over powder made from other methods. HPGA can produce the desired microstructure directly, thus eliminating the need for the long and costly annealing step in the conventional procedure. It also directly generates a fine powder with high surface area, eliminating the need for an additional grinding step. By combining the three steps of melting, heat treatment and grinding used in the conventional procedure into one process HPGA has the potential to significantly reduce the processing cost, one of the barriers to widespread application of AB_2 type Ni-MH batteries.

Metal-Hydride Electrode Requirements

The alloys used as electrodes of high performance Ni-MH batteries must meet a variety of requirements. The first requirement is the amount of hydrogen that it can absorb. This determines the energy storage capacity of the battery and it is measured by amount of hydrogen absorbed per gram of alloy. Secondly, since the electrode operates in a strongly oxidizing alkaline electrolyte, the oxidation and corrosion resistance of the electrodes are critical. Thirdly, reversibility of the battery depends on the bond strength between the metal and hydrogen. Too strong bonds will make the MH electrodes oxidize easily and not be able to store the hydrogen reversibly; too weak bonds lead to alloys that will not react with hydrogen and hydrogen will be released as gas. The optimal bond strength for metal to hydrogen bonds varies from 6 to 12 kcal/mol [12]. Fourthly, rapid electrochemical kinetics and transport processes are essential since they determine the powder output of the batteries. In the discharge process, hydrogen stored in the bulk alloy must diffuse to the electrode surface where it reacts with an hydroxyl ion forming H_2O. This process is determined by both the kinetics of the reactions existing on the electrode-electrolyte interfaces and the hydrogen diffusion rate within the alloy bulk. A typical value of hydrogen diffusion coefficient in the AB_2 type alloy is in the order of 10^{-10} cm_2/s [19].

Metallurgical Characteristics of AB_2 Type Alloy

Although commercialized batteries are predominantly manufactured using alloys of AB_5 type, the excellent properties of AB_2 type alloys make them very promising as superior hydrogen storage materials. An important difference between the AB_5 and AB_2 alloy systems is that the unit cell volume for AB_2 is nearly two times that for AB_5. Consequently,

AB_2 has much lower equilibrium pressures for hydrogen absorption/desorption than that of AB_5 [6]. Another consequence of the unit cell volume difference is that the change in volume caused by the build-up of hydrogen in AB_2 is lower than that of AB_5. This means that alloy pulverization due to the cyclic hydrogen absorption/desorption reaction proceeds much more slowly for the AB_2 type alloys [17]. Moreover, the AB_5 composition contains rare earth elements such as La, Ce, which are expensive elements. Much wider possibilities of composition of AB_2 type alloys may lead to more economical (and extensive) applications [20]. Other advantages include: larger hydrogen reversible capacity, longer cycle life, better corrosion resistance and oxidation resistance. All these advantages make AB_2 type alloys prime candidates for the development of a superior hydrogen storage system.

The composition of the metal hydride alloy is the most widely used way to control the performance of the materials as regards pressure, rate cycle life, low temperature performance and charge retention. In general, Nickel is the basic component in most of the current hydrogen storage materials. Besides nickel, an AB_2 type alloy consists of combinations of various elements and may contain as many as 10 elements, with the maximum amount of any one element being $\approx 30\%$ [5]. The wide range of physical and chemical properties that can be produced in these alloys allows the MH battery performance to be optimized.

Each element in the multicomponent alloy has a role in improving the performance of the electrode. The function of the A component is to create a stable hydride. The elements that are used to increase hydride stability include Zr, V and Ti. The B component has multiple functions, including 1) improving the hydriding-dehydriding characteristics, 2) adjusting the equilibrium pressures for the hydrogen absorption/desorption to desire levels, and 3) enhancing the stability of the alloys and preventing the A components form being readily oxidized [6]. Therefore, transient elements which do not have completely filled d orbitals, such as Ni, Cr, Fe, Mn, V, Al, Si, Mo, Co, are usually selected as the B component.

The optimum microstructure for AB_2 cathode materials is a highly disordered multiphase mixture of amorphous and crystalline region [21]. This is in contrast to the optimum microstructure for AB_5 type materials, which is a homogeneous, equilibrium hexagonal single phase [22].

The AB_2 type alloys belong to the class of materials known as Laves phase [5]. These phases are a group of topologically highly close-packed intermetallic (t.c.p.) compounds with an AB_2 stoichiometry. Typically, the Laves phases are categorized into one of three crystal structures based on magnesium: $MgCu_2$-type structure (cubic C15 or 3C), $MgZn_2$-type structure (hexagonal C14 or 2H) and $MgNi_2$-type structure (dihexagonal C36 or 4H) [23]. C14, C15 and C36 are the Strukturicht Symbols, in which capital C represents AB_2 type compounds [24]. The C14 and C15 structures are the most frequently encountered. Polytypes based on these three structures also can be found in some intermetallics.

A atoms are much larger than the B atoms in Laves phases. Laves demonstrated that in all AB_2 type compound the AA and the BB separation are smaller than the AB separation. In the hard sphere model like atoms touch each other [25]. In practice, substitution of A sites or B sites are often used to produced multiple phase alloys.

Some studies [5, 26,] demonstrated that the AB_2 type alloys consist of both C15 and C14 Laves phases. Apart from the C14 and C15 structures, it is also quite common that this material contains other bcc and hexagonal phases [11].

In this study, an alloy of AB_2 type having base on the Zr-Ti-Ni-Mn-V-Cr was investigated. In previous X-ray powder diffraction study [27], the Rietveld refinement analysis was been carried out for phase identification and phase abundance on our material. The results indicated that these alloys consisted of two main phases, cubic C15 with lattice parameter of a=7.031(1) Å and hexagonal C14 phase with lattice parameter a=4.973(2) Å, c=8.111(4) Å. The C15 structure belongs to the space group Fd3m (No.227) and Pearson symbol cF24 [28]; The C14 structure belongs to the same space group $P6_3/mmc$ (No.194) and Pearson symbol hP12 [28]. The C14 structure contains 12 atoms per unit cell and C15 contains 24 atoms.

Statement of Work

At the present, a wide variety of alloys with different compositions have been tested and the synthesis and electrochemical activity of these alloys studied [29-37]. Most of the work has concentrated on (i) preparing alloys of AB_2 type by using the arc-melting/annealing and mechanical alloying/annealing techniques etc; (ii) determining the hydrogen absorption/desorption behavior (pressure-composition isotherm as a function of temperature) and (iii) evaluating their performance characteristics as hydride electrodes (charge/discharge, capacity retention, cycle life, high rate capability).

The alloys of AB_2 type used for electrode manufacture are predominantly polycrystalline and multiphase by design. It is generally accepted that the performance of the batteries is closely related to the crystal characteristics and phase assemblage of the alloy. The crystalline structure and occurrence of individual phases are sensitive to the alloy composition. Therefore, a better understanding of the nature of the alloys, the condition of existence of each phase and the relationships between these phases is necessary. However, little work has been done examining their physicochemical characteristics (morphology, composition); no attempts have been made on characterizing and understanding the microstructure of AB_2 type alloys using transmission electron microscopy thus far.

The purpose of this research was to study the nature of individual phases; the condition of appearance of particular phases and the phase abundance and distribution of the elements in the multiple phases using TEM. In this study, an emphasis was placed on the powder prepared by HPGA in both as-atomized and heat treated condition.

EXPERIMENTAL PROCEDURE

The specific alloy studied in this investigation is a multicomponent AB_2 type hydrogen storage alloy based on the Zr-Ti-Ni-Mn-V-Cr system, with the Ti/Zr ratio being approximately 1/3, and the Ni/Mn ratio being 7/3. Small amounts of Cr and V are added to improve the alloy performance. The exact composition can not be given due to proprietary restrictions. A list of the alloy powders examined in this study is found in Table 2.

Table 2. A list of powders investigated in this study.

Powder ID	Preparation/Description
Chill Cast	Chill cast ingot, starting material of HPGA
HDH	Hydride-dehydride process; commercial available
HPGA	High pressure gas atomization by Argon
HT	Heat treatment at 985^0C for 30minutes after HPGA

The HPGA powder was produced by the Ames Laboratory high pressure gas atomization process. A large chill cast ingot was used as the starting material for the melt. The powder was screened with wire mesh sieves into size class of diameter <45um. Some powder was sealed in a quartz vial under an Ar atmosphere and subjected to heat treatment in a box furnace at 985^0C for 30 minutes in order to eliminate the composition segregation. The annealing process was not to homogenize the microstructure and enhance crystalline perfection, but to produce a partially crystallized microstructure which is claimed to improve the properties of the AB_2 alloy [11]. The starting chill cast ingot was also crushed into small pieces and examined, as well as the commercialized HDH powder. The HDH powder was prepared by the single reaction of hydrogen absorption and desorption, a hydride - dehydride (HDH) process, to fracture a large ingot into smaller pieces.

X-ray diffraction (XRD) studies of the material were conducted using a Philips PW 1830 generator operated at 40 kV and 20 mA. Cu K_α radiation ($\lambda = 1.5406Å$) was used in XRD.

The SEM samples were prepared by mounting and polishing followed by a very thin gold coating before examination. An Amray 1845 field emission SEM, equipped with an Oxford 5478 energy dispersive X-ray spectrometer (EDS) unit, was employed to examine the powder. An analysis of the morphology, composition and distribution of the elements in the powder was made by EDS technique.

The TEM sample preparation of the HPGA material involved gluing powders onto a 200-mesh copper grid using epoxy. After the epoxy hardened the grids were mechanically ground and dimpled to perforation followed by ion milling using 5 keV Ar ions in a Gatan ion miller on the cold stage for 20 minutes or less. Ion milling for longer times was found to cause the epoxy to smear across the sample. This method was time consuming but yielded the best samples. TEM studies were performed using a Philips CM30 STEM equipped with a liquid-nitrogen-cooled double tilt sample holder and an Oxford Link Analytical 5720 EDS unit operating at 300KV. The microanalysis was performed with a 52nm (Full Width at Half Maximum) diameter electron probe. Compositions (atomic%) were determined from the data using the Cliff-Lorimer standardless ratio technique [38] in the software DTSA from the National Institute of Health.

EXPERIMENTAL RESULTS

X-ray Diffraction

The results of x-ray diffraction analysis on the powders are shown in Figure 2. As seen in a previous study [27], the patterns are similar in that there are two main phases, C15 and C14, with the predominant phase being C14. However, some differences are apparent between the scans of Figure 2. Peak broadening was seen in the XRD patterns of the HPGA powder, indicating a smaller grain size and/or possibly the existence of strain in the material. The HDH powder has several small peaks in the region 38-42° two-theta (circled). Phases identified that produce peaks at these locations include ZrO and a Mn-Ni-Zr hydride [39].

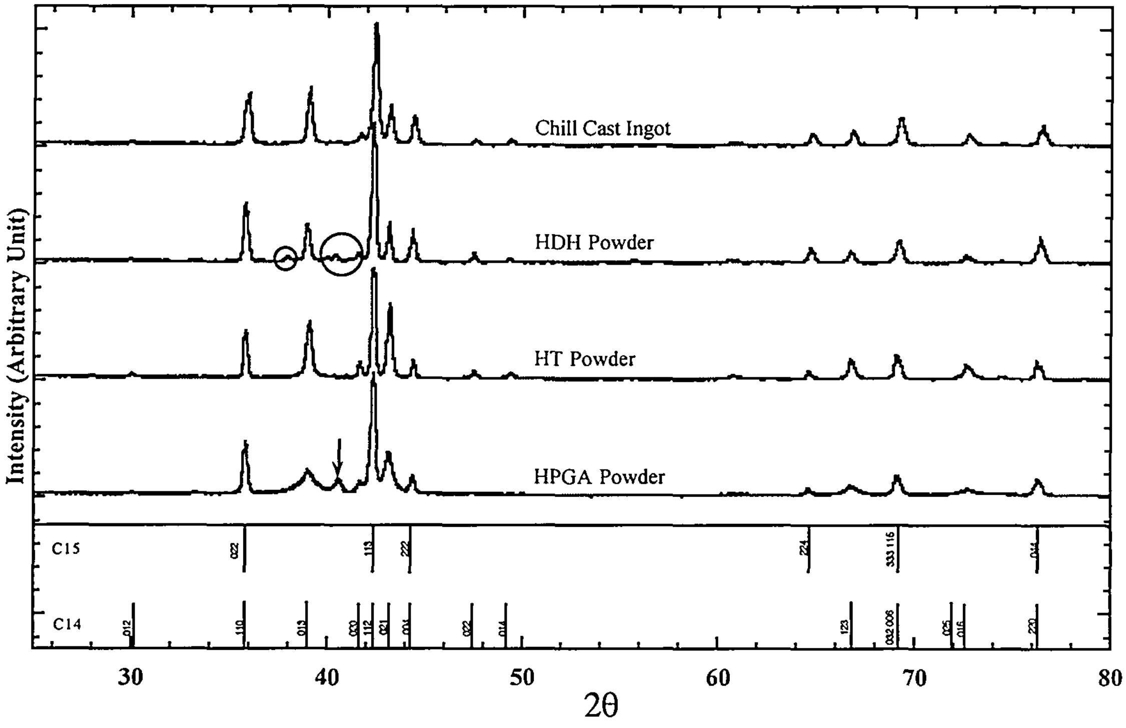

Figure 2. XRD Patterns obtained from material examined in this study.

The HPGA powder has one extra peak present at 41.1° two-theta (arrowed). The heat treated powder has no such extra peak, all those present belong to the C14 or C15 structures. The peak width decreased upon heat treatment, indicating either grain coarsenings or strain reduction.

Scanning Electron Microscopy

The microstructure of a cross-sectioned sample of the chill cast starting material is shown in Figure 3a. The structure appears to consist primarily of large grains of a single phase with an approximate composition $Zr_{27}Ti_{10}Ni_{41}V_4Mn_{14}Cr_4$. SEM observations revealed the existence of a few Sn-rich impurities in the chill cast ingot and in as-atomized powder. These impurities exist as a scattering of small inclusions (circled). The EDS analysis reveals the inclusions to be Sn rich with an approximate composition $Zr_{26}Ti_{12}Ni_{38}Mn_4Sn_{20}$. The extra peak in the XRD of as-atomized powder may be due to this Sn-rich phase.

The HDH particulate appears as irregular chunks of average size 20μm (Figure 3b). The overall scan shows that the main phase composition is close to $Zr_{28}Ti_9Ni_{38}V_5Mn_{15}Cr_5$. In addition, a nearly 93% Zr was observed by EDS.

The HPGA material in the as-atomized condition consists of uniform spherical powders of size –45μm (Figure 4a). Cross-sectioned samples of the as-atomized powders, Figure 4b, reveal a number of phases present in small amounts in the as-atomized condition. These include: 1) the major phase with approximately composition $Zr_{28}Ti_9Ni_{36}V_5Mn_{17}Cr_5$; 2) large amounts of a phase with composition $Zr_{32}Ti_{13}Ni_{53}$; 3) a minor phase with composition ZrNiSn, and 4) occasional regions containing 95% Zr.

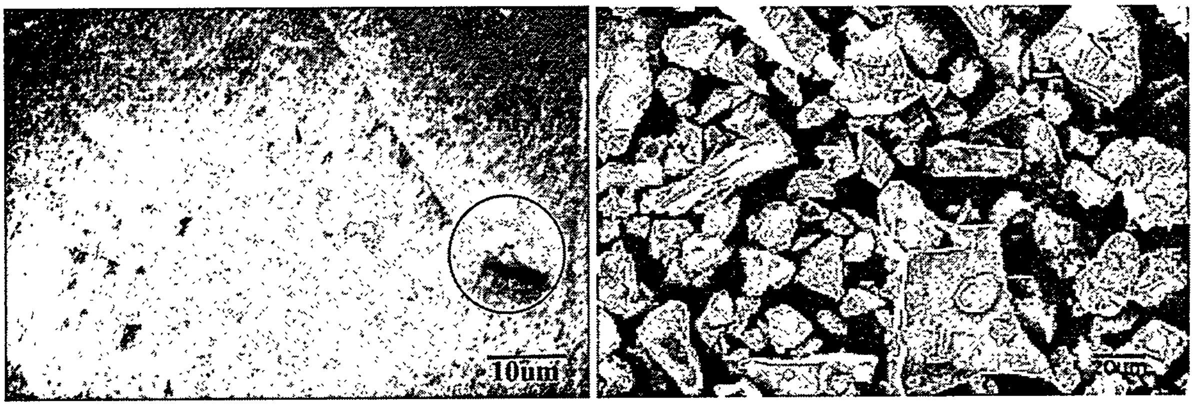

a. b.

Figure 3. a) The chill cast powder shows Sn rich inclusions (circled); b) The morphology of the HDH powder shows irregular shape.

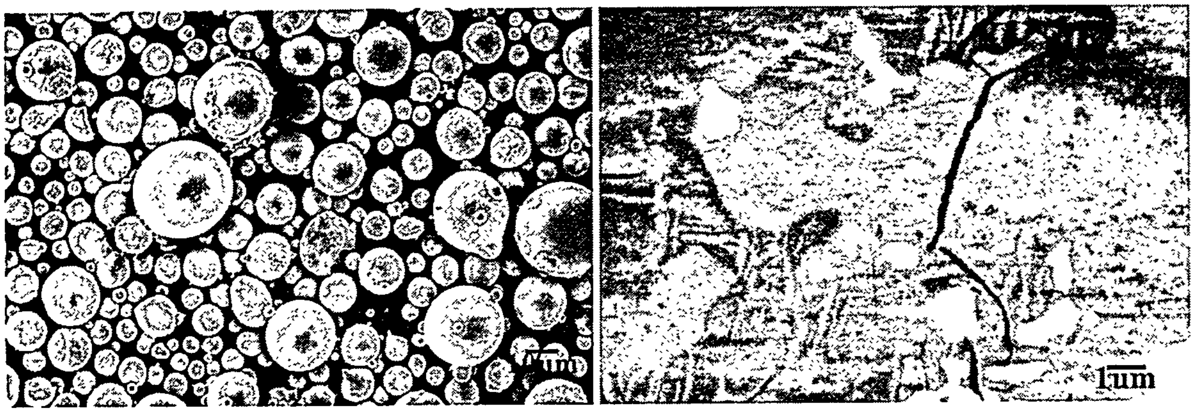

a b.

Figure 4. a) The as-atomized powder shows spherical shape; b) A cross-sectioned as-atomized powder.

The surface morphology of the powders appears unaffected by the heat treatment (Figure 5a). SEM/EDS analysis indicates that the heat treated powder is much more uniform in microstructure (Figure 5b). The EDS overall scan indicates the same composition as the nominal composition. There are some small particles scattered throughout the matrix; these particles were also observed and analyzed using TEM.

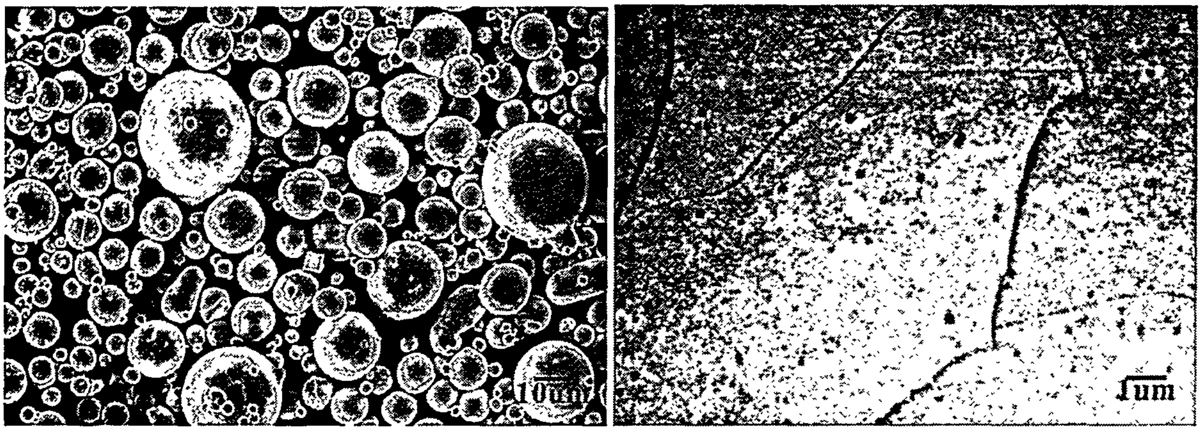

a. b.

Figure 5. a) Powder in heat treated condition; b) A cross-sectioned heat treated powder.

Transmission Electron Microscopy

TEM was used to investigate the microstructure of the HPGA material in both as-atomized and heat treated condition. Figure 6 is a montage of TEM micrographs showing an HPGA powder that was thinned sufficiently to enable the entire microstructure to be seen. Figure 7a shows that the solidification structure is dendritic, with the dendrites having a heavily faulted structure (Figure7b). The direction of the fault structure is consistent within each individual dendrite arm, giving the false appearance that they are continuous across the secondary arms through the interdendritic region. Selected Area Diffraction (SAD) patterns from the faulted dendrites are shown in Figure 8. These patterns can be indexed as a combination of the C14 and C15 structures. The software Desktop Microscopist was used to generate the electron diffraction from the C14 and C15 phases. These computer generated SAD patterns (also in Figure 8) are coincident with those taken on the TEM. The Orientation Relationship (OR) between the two structures was determined to be $(111)[1\bar{1}0]_{C15}//(0001)[11\bar{2}0]_{C14}$

Figure 6. Montage of TEM micrographs showing the microstructure through one-half of an as-atomized powder.

The lattice constants were determined to be a=7.03Å for C15 phase, while a=4.97Å, c=8.11Å for the C14 phase. This result is consistent with that from XRD study [27].

A second phase can be seen in the interdendritic regions, with the average width being about 20nm (Figure 9a). Quantitative metallography shows 8% volume fraction of this phase. Convergent beam electron diffraction (CBED) of the interdendritic structure showed hexagonal symmetry (Figure 9b) and is identified as the C14 phase.

While not apparent in Figure 6, some powders exhibited small polycrystalline regions (Figure 9c) scattered through out the sample. SAD patterns from this region (Figure 9d) consist of a number of rings. The breadth of the diffraction rings makes precise measurement of the d-spacing difficult. However, the d-spacings closely matched those of the C14 phase. The d-spacings are listed in Table 3.

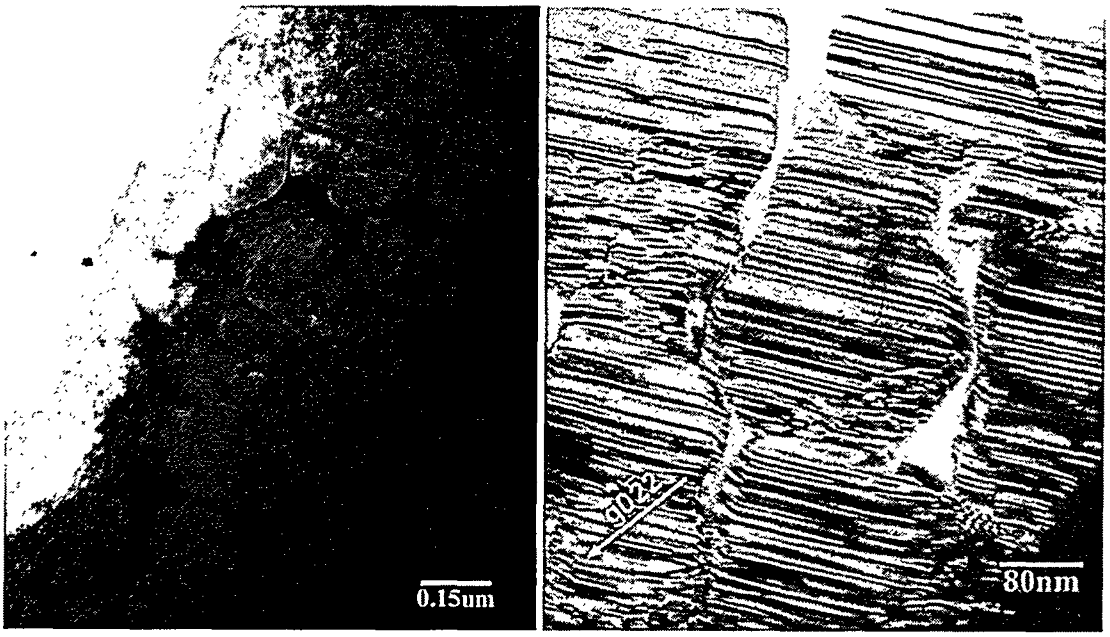

a. b.

Figure 7. Microstructures of as-atomized powder: a) low magnification of dendrite region; b) tilt orientation showing the faults within the dendrite arm.

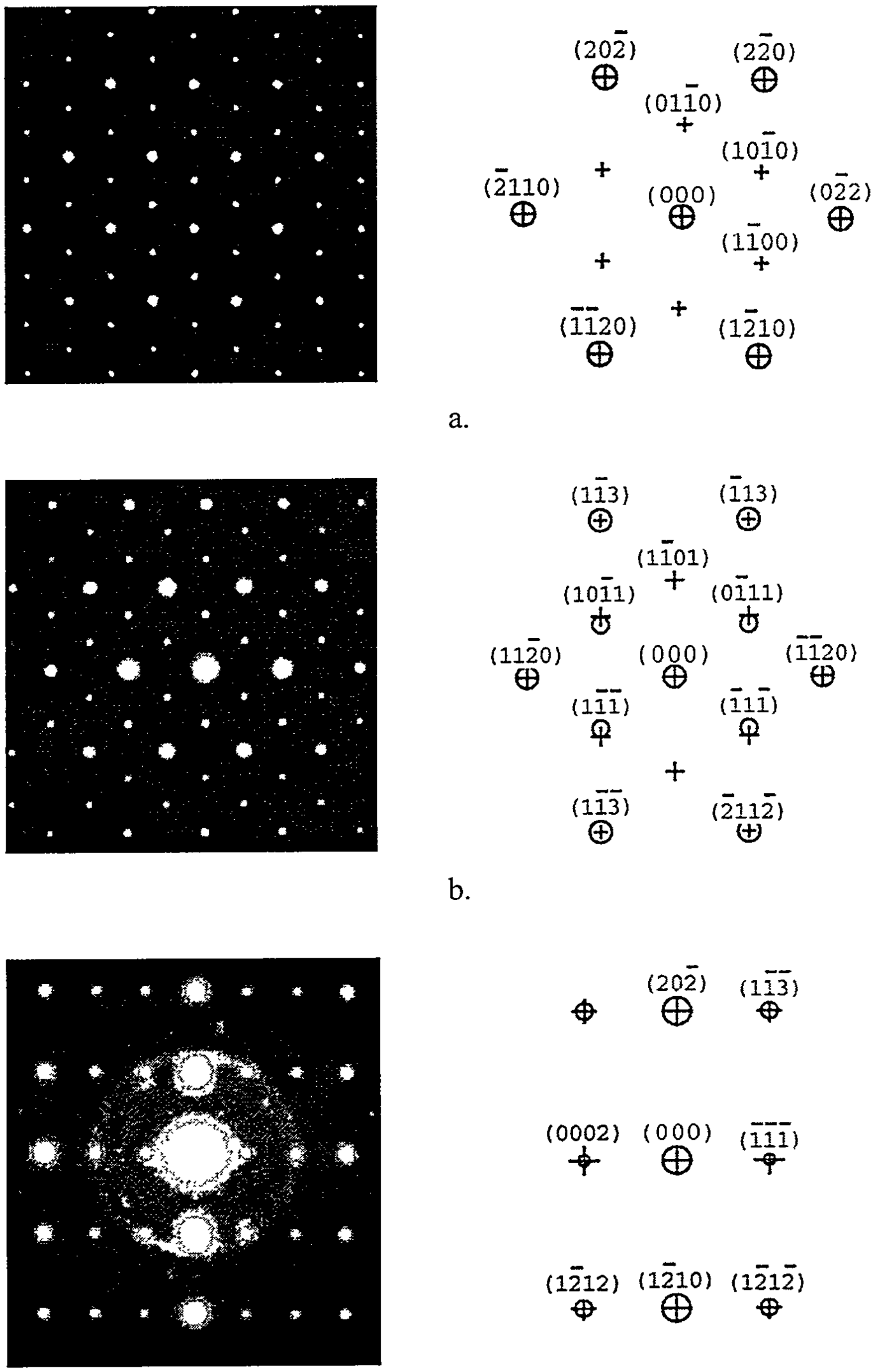

Figure 8. SAD patterns and the computer generated diffraction patterns (O: the diffraction spots from C15; +: the diffraction spots from C14) from the dendritic region show a combination of C14 and C15 structures): a) [111] zone; b) [011] zone; c) [112] zone.

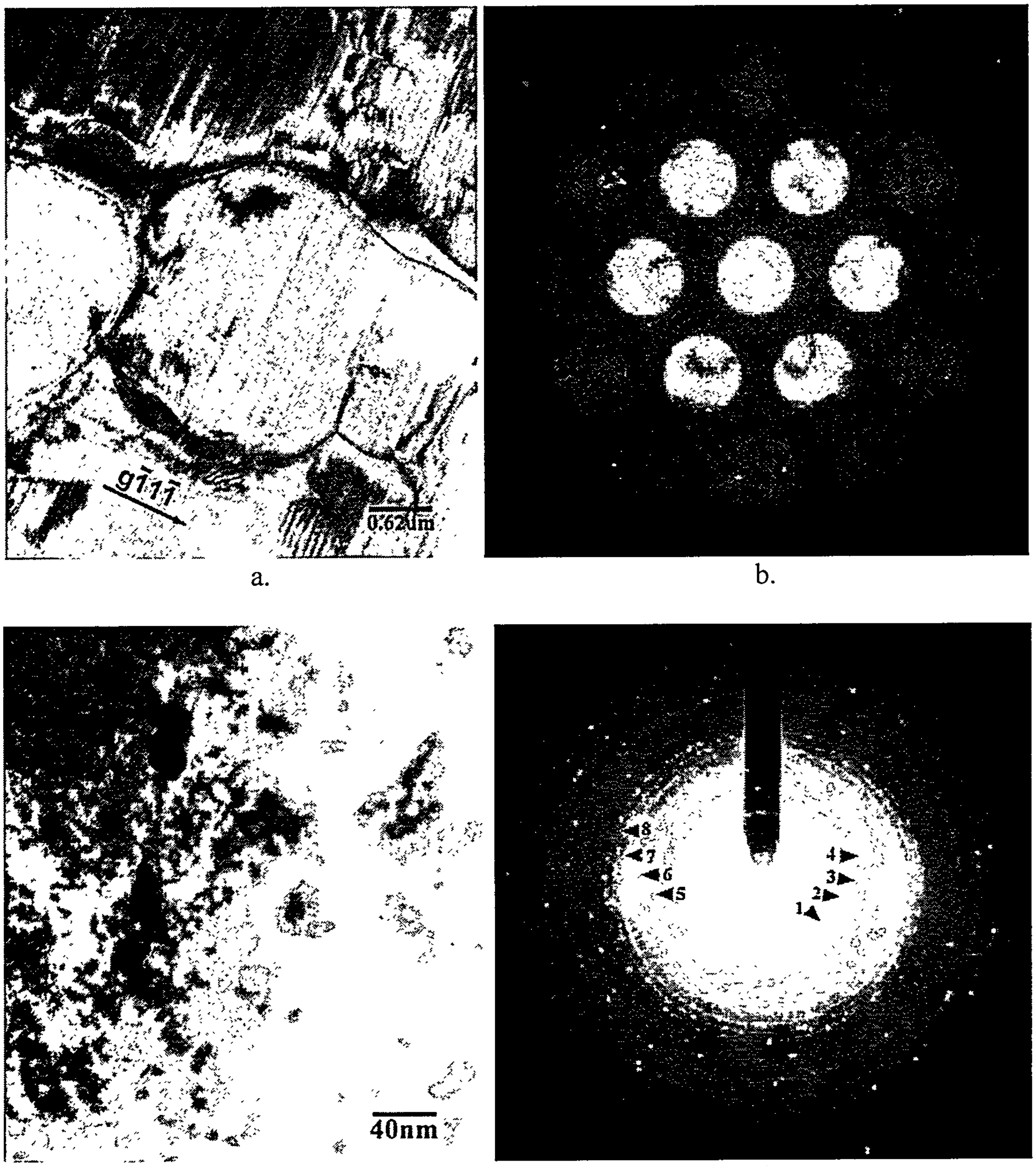

a.

b.

c.

d.

Figure 9. Microstructures of as-atomized powder. a) high mag showing the dendrite arm and the interdendritic phase; b) CBED [0001] zone pattern from interdendritic region shows hexagonal symmetry; c) typical polycrystalline region in the powder; d) diffraction rings from the polycrystalline region.

Table 3. The index of the diffraction rings of HPGA powder.

Ring No.	d- Spacing (Å)	C14
1	3.802	(011)
2	3.009	(012)
3	2.471	(110)
4	2.247	(013)
5	2.072	(112)
6	1.912	(022)
7	1.831	(014)
8	1.601	(121)

After heat treatment, the HPGA material showed several microstructure changes that correlate with the XRD data shown earlier. The overall microstructure differed from those of the as-atomized material although it still consisted of three distinct features or regions. Firstly, the dendritic structure evident in HPGA powder was replaced by a large, fairly equi-axed grain structure (Figure 10a), the average grain size being 1 μm. The large grains still exhibited a faulted structure, as did the dendrites. However, the nature of the faults had changed. They now were very defined and appeared as intercalation layers of C14 and C15 phases within the grains, Figure 10b. The CBED patterns from Figure 10b are shown in Figure 10c-d. The regions where these patterns were obtained are marked. The majority of the grain consisted of the hexagonal C14 structure as shown in Figure 10c. When the beam was placed on the intercalation layer marked as A the cubic C15 crystal structure was seen (Figure 10d). These results clearly show that the grains themselves consist of both the C14 and C15 structures. The interdendritic phase no longer existed, being replaced by discrete, roughly spherical particles scattered at the grain boundaries (arrowed in Figure 10e). These particles had an average diameter of 0.3um. One such particle is shown in Figure 10f.. The polycrystalline region observed in the as-atomized material was still present (Figure 10f) in some powder after heat treatment and the grains may have coarsened slightly. The SAD patterns show that this region now consisted of both C14 and C15 structures (Table 4).

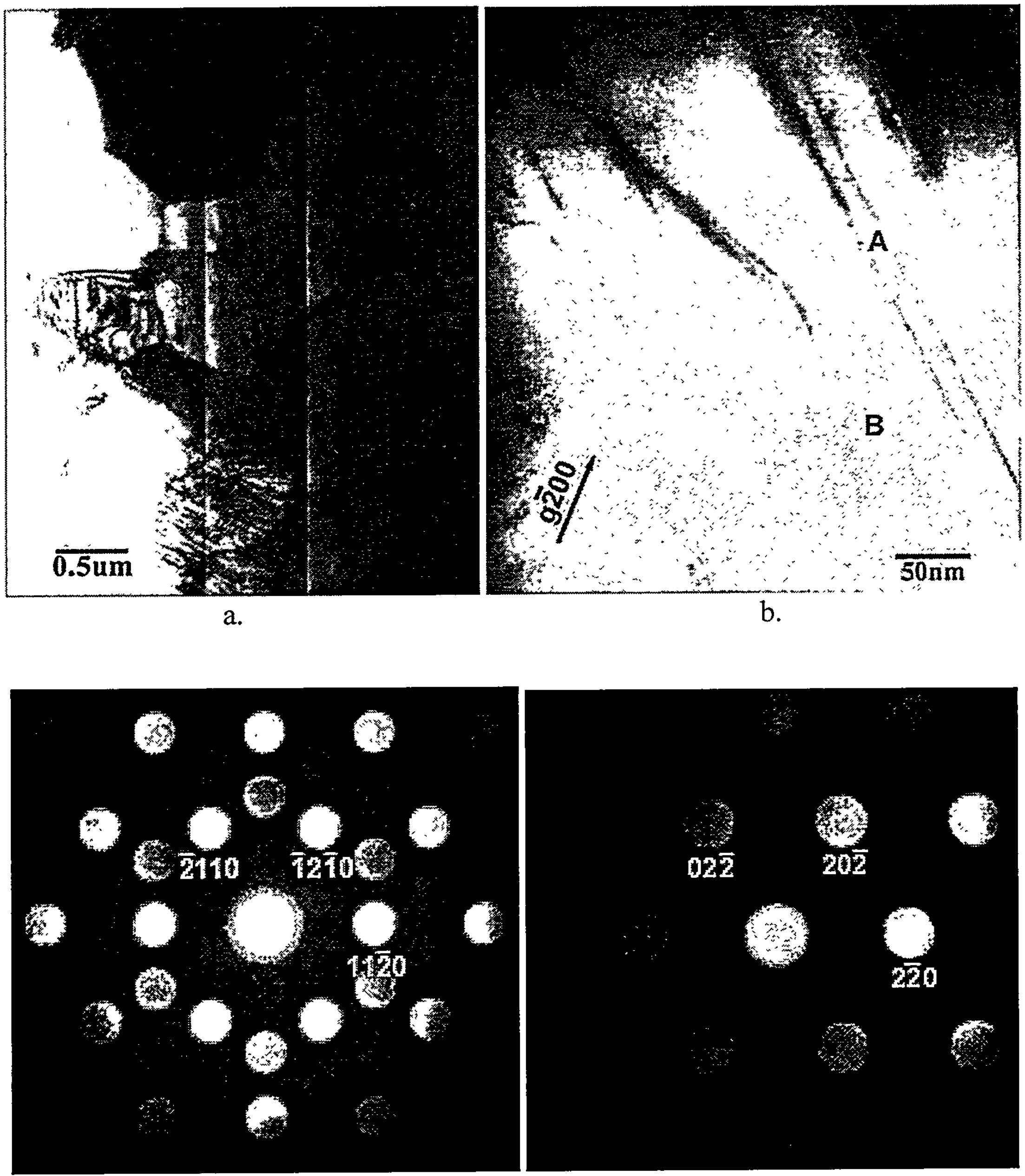

a. b.

c. d.

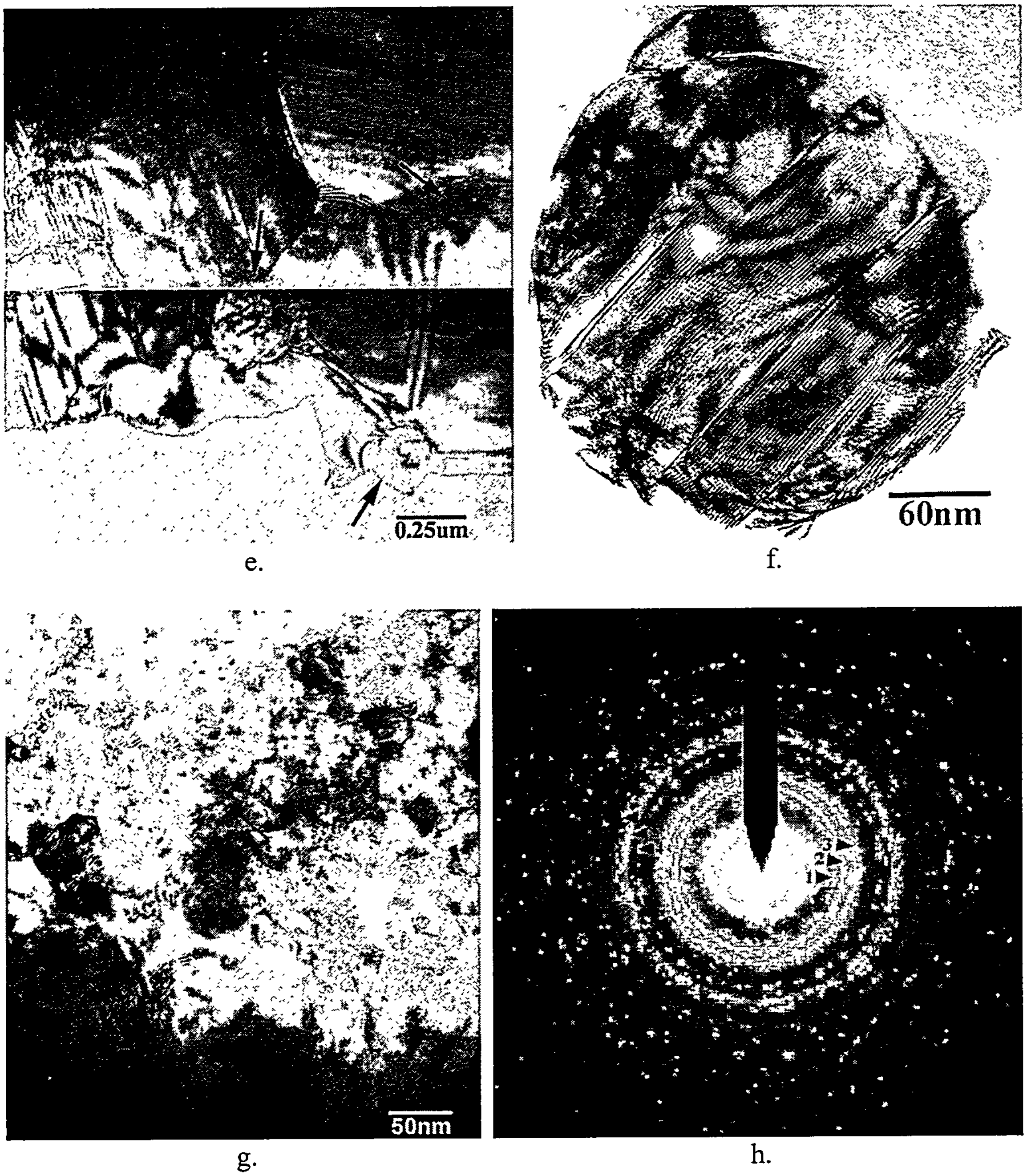

Figure 10. Powder in the heat treated condition. a) Equi-axed grains; b) The intercalation layers in the heat treated powder; c) The CBED pattern from region B; d) The CBED pattern from the region A; e) Particles at a grain boundary triple point; f) A high magnification image of a particular particle; g) the polycrystalline region in the heat treated powder; h) the diffraction rings from the polycrystalline region;

Table 4. The index of the diffraction rings of heat treated powder.

Ring No.	d- Spacing (Å)	C14	C15
1	2.908	(012)	N
2	2.563	(110)	N
3	2.203	(020)	N
4	1.765	N	(004)
5	1.617	N	(133)
6	1.504	(122)	N

Phase Composition

The EDS measurements indicate that in the multi-phase alloys each region has a specific composition, which is different from the bulk stoichiometry. The EDS spectra obtained using the TEM for as-atomized and heat treated powder are shown in Figure 11. Only K lines are labeled in these spectra. An accelerating voltage of 300 kV and a probe diameter of 52 nm maximum (smaller than the size of the phases examined) was used for all scans. Note that the relative amounts of Zr, Ti, V, Mn and Cr changes, with the interdendritic phase being depleted in V, Cr and Mn and enriched in Ti and possibly Zr. The amount of Ni remains approximately the same in both regions. The quantative EDS results are listed in Table 5. The composition of the faulted grains in the heat treated powder is near that of the as-atomized powder. However, a large difference is observed between the particles scattered on the grain boundaries and the interdendritic phase, from whence they presumably originated. The particles are rich in Zr and Ni and depleted in the remaining elements. A spectrum obtained from one such particle is shown in Figure 11c.

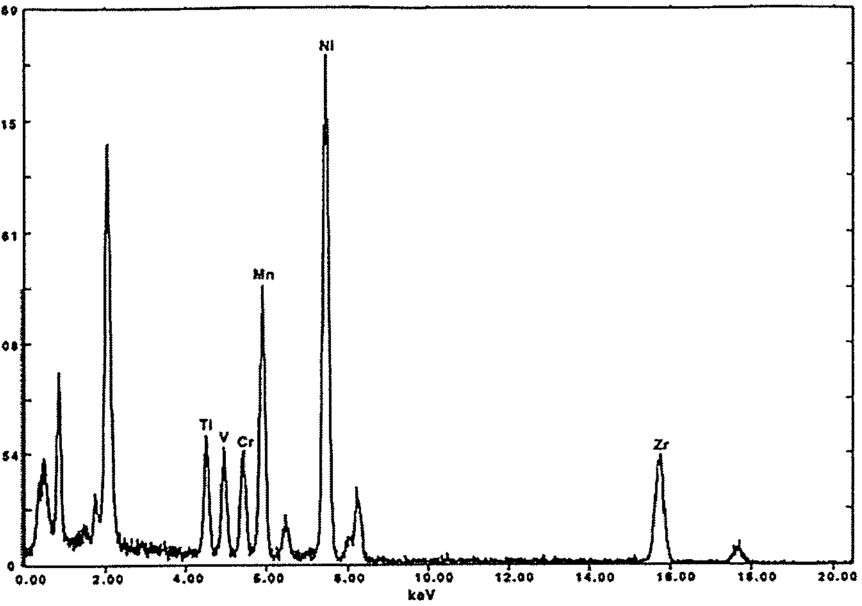
769
615
461
308
154
0
Ni
Mn
Ti
V
Cr
Zr
0.00
2.00
4.00
6.00
8.00
10.00
12.00
14.00
16.00
18.00
20.00
keV

a.

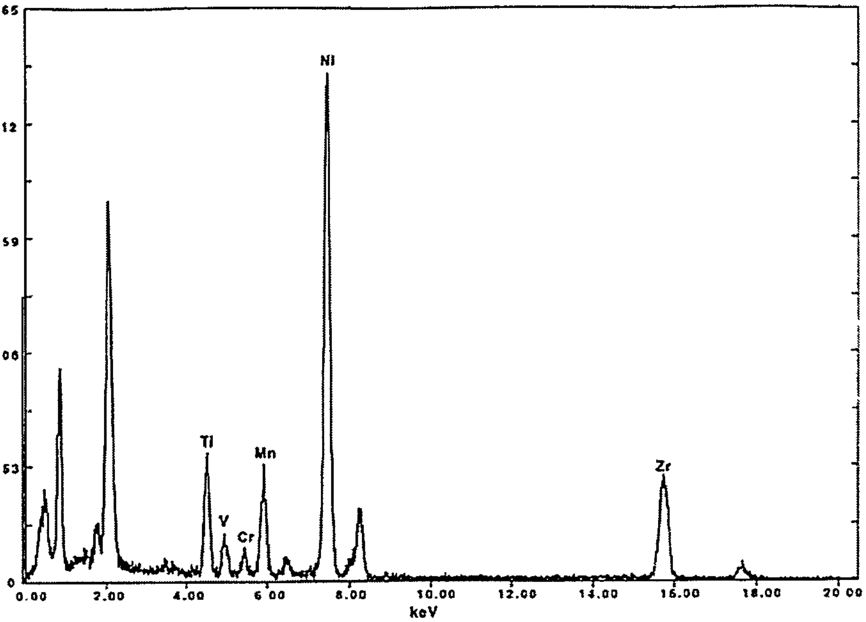
765
612
459
306
153
0
Ni
Ti
Mn
V
Cr
Zr
0.00
2.00
4.00
6.00
8.00
10.00
12.00
14.00
16.00
18.00
20.00
keV

b.

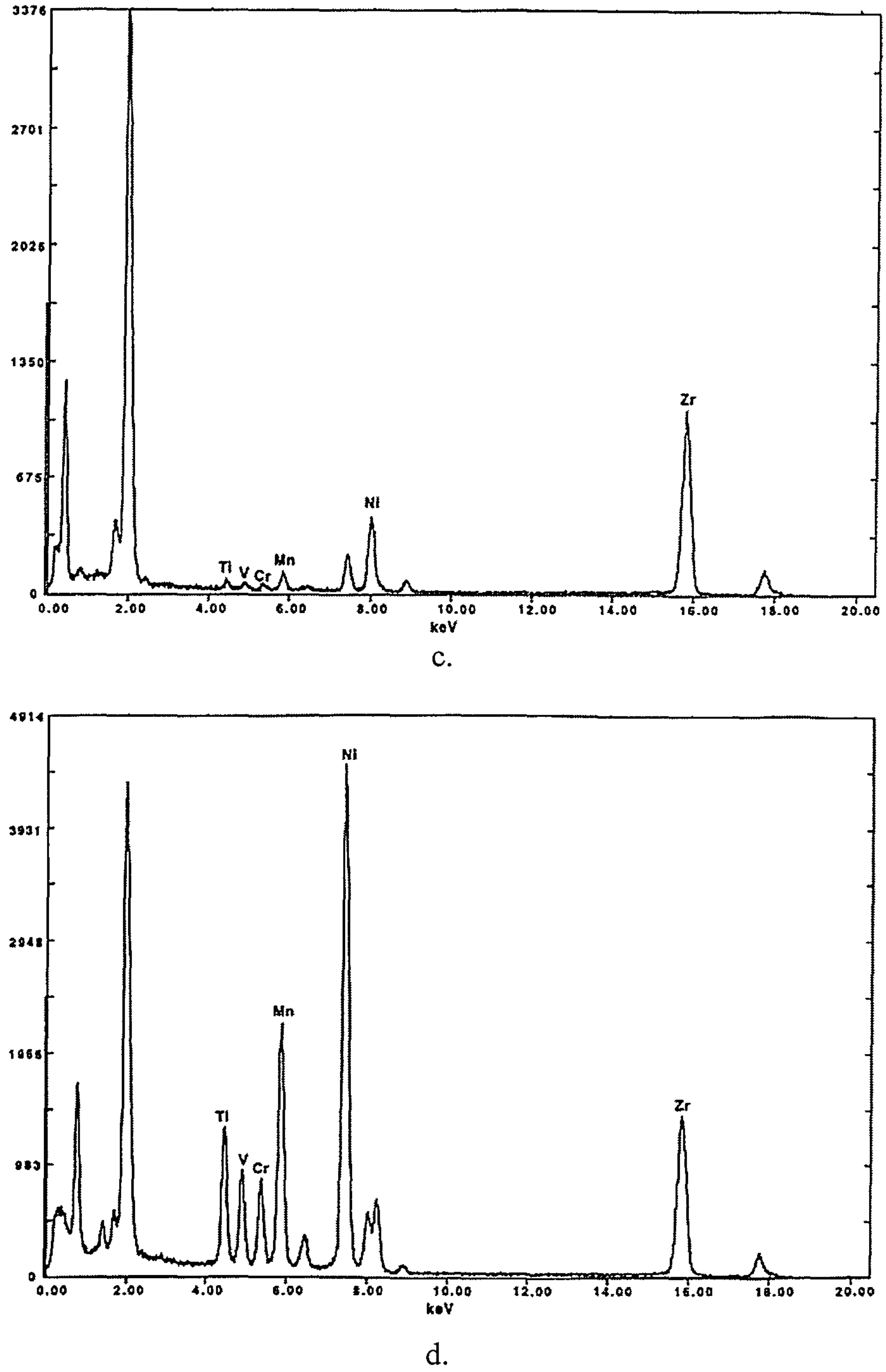

Figure 11. EDS spectra from a) Large faulted dendrites of as-atomized powder; b) Interdendritic regions in as-atomized material; c) Spherical particles in heat treated material; d) Grains of the heat treated powder.

Table 5. The EDS quantitative result of different regions in as-atomized powder*.

Examined Region	Elements Concentration (at%)					
	Zr	Ti	Ni	Mn	V	Cr
Dendrite	9.67	12.71	33.98	23.63	9.70	10.31
Interdendrite	12.37	20.29	34.15	19.13	4.86	6.49

*The exact number can not be given due to proprietary restrictions

DISCUSSION

Heat Treatment Effect

Many phases were observed in the HPGA powder using the SEM but no evidence was seen of their existence in the XRD data. There are several possible explanations for this. The phases seen in the SEM might be composition variations of the C14 and C15 structures noted in the XRD data. Many of the peaks for these structures overlap, as do peaks for the C36 Laves phase structure. It is also possible that the phases detected using SEM comprise a small volume percentage of the whole sample. Depending on the structure factor, as much as 5-10% impurity levels can exist in XRD samples without significant diffraction being detected. There is no evidence from the TEM work of phases existing in the as-atomized powder that may account for the extra peak. However, only a limited amount of material can be examined in the TEM, so this is not surprising.

The TEM studies indicate that a polycrystalline region coexists with the main phases in the atomized powder. During gas atomization, the liquid alloy was sprayed and quenched by Argon in the moment of leaving the nozzle, and the solidification rate is normally over 1000°C s^{-1}. It is possible that a polycrystalline layer might exist on the particle surface due to such a high solidification rate, similar to a chill region in a cast ingot. The number of powders observed in TEM containing the polycrystalline region was relatively low, so it is assumed to have little or no effect on the hydrogen storage properties of the material.

Upon heat treatment the interdendritic phase seen in the as-atomized material appears to be substantially consumed in a reaction with the existing dendrite. This reaction has two results. Firstly, the fault structure that exists within the grains becomes more defined and appears as layers within the grains. Distinct C14 and C15 phase regions were not seen in the TEM samples, rather the observed layers are believed to be intercalation layers consisting of alternating C15 and C14 structures were observed. Secondly, a new phase rich in Zr and Ni appears in the form of spherical particles present at the grain boundaries. The small number of Zr/Ni rich particles that remain after the heat treatment would result from the development of the intercalation layers since slight changes in composition are necessary to accommodate the alternating structure observed. Finally, the polycrystalline region, lightly coarsened, now consists of a mixture of both the C15 and C14 phases. The effect the polycrystalline region on the above reaction is believed to be negligible.

It is claimed [40] that some electrochemical properties of the AB_2 materials are improved upon heat treatment. The improvement after heat treatment has been explained by the improvement of the crystallization of the powder and variation of the atomized powder surface. The increase in C14 phase volume has also been suggested as another contributing factor, because the larger tetragonal interstitial site (TIS) in the C14 hexagonal structure is beneficial to hydrogen storage capacity [37].

Crystallography and Orientation Relationship

The Laves phases are closed-packed and closely related to one another. The real lattices of Laves phase variants C14, C15 and C36 are shown in Figure 12. In order to illustrate clearly the three structures in terms of stacking of hexagonal layers in Laves phases structures, the C15 structure is displayed along the [111] direction of the cubic unit cell, while the C14 and C36 structure are shown along the [0001] directions. The atomic structures (coordination polyhedra) in these Laves phases show a marked similarity [41]: A is

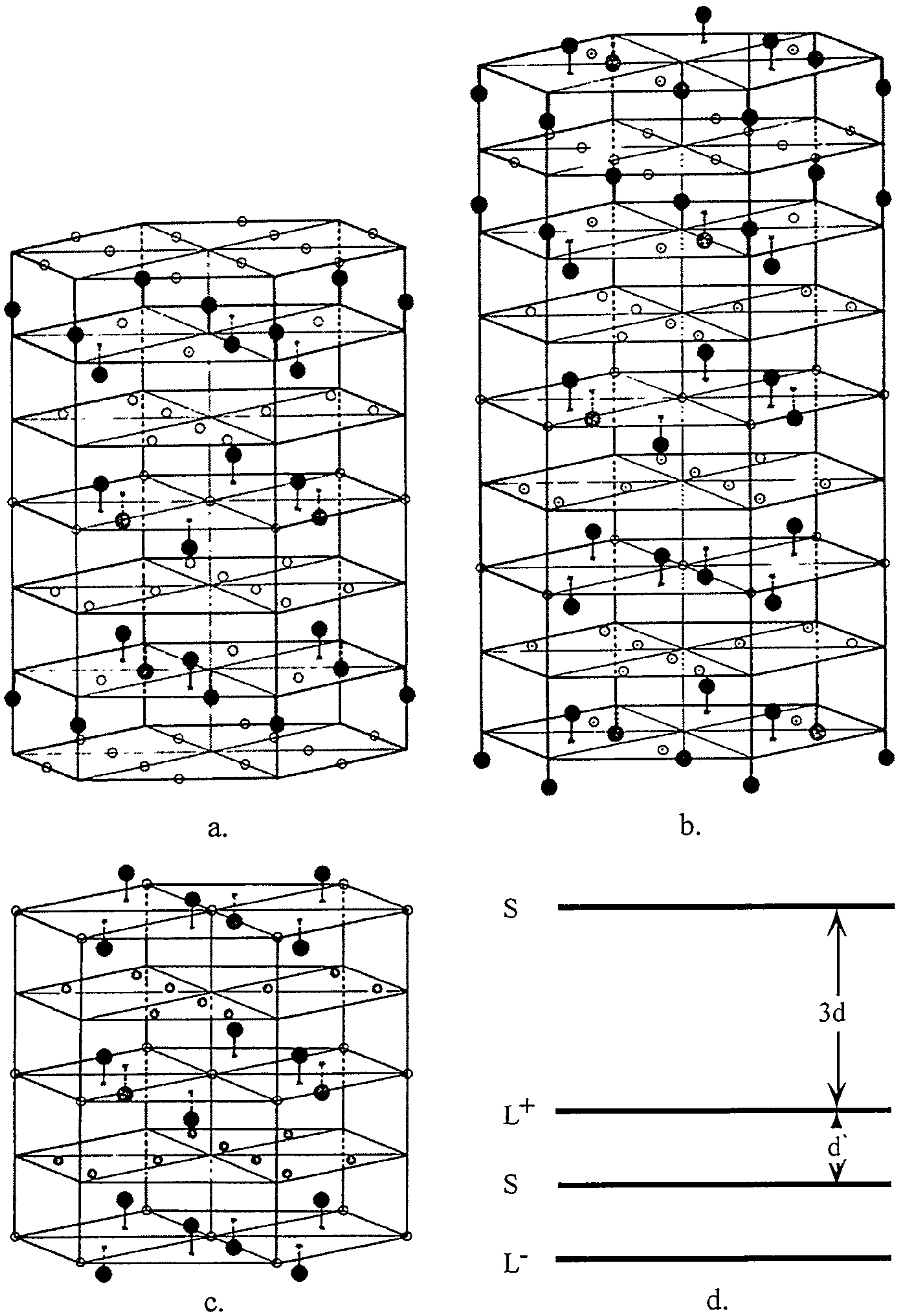

Figure 12. The (a) C15, (b) C36 and (c) C14 crystal structure (after [41]); (d) Alternation of single layers with triple layers and also of large L and small S atoms (after [42]). L^+ represents the A atoms above the B atom plane, L^- represents the A atoms below that plane.

surrounded by 4 A and 12 B atoms and B is surrounded by 6 A and 6 B atoms; the nearest neighbor distances are also identical in the three structures. However, these structures differ in the stacking sequences.

In Laves phase structures, each stacking layer consists of an interpenetrating single layer of small atoms and a triple layer [Figure 12d] in two variants, and thus they are called quadruple layers. These layers form the basal planes of the crystal structures and may be shifted by three Burgers type vectors relative to each other that can be labelled X, Y, Z. For each layer two variants exist, e.g. X and X' which are twin related. The layers stacked sequentially follow a certain stacking rule [43]: above a plain layer, the stacking sequence is XYZ; above a primed layer, the sequence is XZY. According to this rule, various ordered structures can be obtained depending on their stacking sequence. The full stacking sequences can be expressed as:

C14 (2H) $$\frac{\alpha A\alpha c\ \ \beta B\beta a}{X \qquad Y}\cdots;$$

C15 (3C) $$\frac{\alpha A\alpha c\ \ \beta B\beta a\ \ \gamma C\gamma b}{X \qquad Y \qquad Z}\cdots;$$

C36 (4H) $$\frac{\alpha A\alpha c\ \ \beta B\beta a\ \ \alpha A\alpha b\ \ \gamma C\gamma b}{X \qquad Y \qquad X' \qquad Z}\cdots.$$

The Greek letters denote the layers containing large A atoms, the Latin letters denote layers containing small B atoms and X, Y, Z represents the possible stacking sequences for the four layer groups. This stacking sequences leads to values of axial ratios in the proportions 2 : 3 : 4 for C14 : C15 : C36. Referring to Figure 13 and lattice constants of our materials, these axial ratio produce real lattice distances of ≈ 8Å, 12Å and 16Å respectively. Other polytypes with longer periodicity also exist, e.g.5R with sequence XYZX'Z, 6H with

XYZ'Y'XY' etc. These structures can be considered as containing various shorter periodicity stacking structures, for instance, 16H=4H+4H+4H+2H+2H. The structures of various Laves phase types are so similar that they can easily shift from one to another with only minor changes in composition.

A simple calculation will give a clue that the C14 and C15 in our materials are highly related. The adjacent quadruple layers spacing is:

$$d_{C15} = a \times \frac{\sqrt{3}}{3} = 7.031\text{Å} \times \frac{\sqrt{3}}{3} = 4.059\text{Å} \text{ for the C15 structure;}$$

$$d_{C14} = \frac{c}{2} = \frac{8.111\text{Å}}{2} = 4.056\text{Å} \text{ for the C14 structure.}$$

These two values are nearly equal. (Lattice constants were after [27]).

The superimposed stereograms (Figure 13) of the two structures illustrate the good orientation relationship that exists between them. The orientation relationship between the two structures was determined to be $(111)[1\bar{1}0]_{C15}//(0001)[11\bar{2}0]_{C14}$. The same orientation relationship between the C15 and C14 Laves phases was also observed in a Zr-Mn-V-Ni AB_2 type alloy [44]. Therefore, close parallel exists between the two crystal systems, i.e. the close-packed planes in one crystal are parallel with those in the other crystal. This, along with the almost identical lattice constants, implies an easy transition between the two phases.

Figure 13 is a high resolution TEM micrograph showing a particular grain. The intercalation layers are clearly seen and can be measured. Three different layers can be identified having spacing 8Å, 12Å and 16Å. Thus, it appears that rather than a simple structure consisting of C14 and C15 structures, several possible structure types can coexist. While the major phase is C14, the C15 and C36 structures are also present in minor amounts.

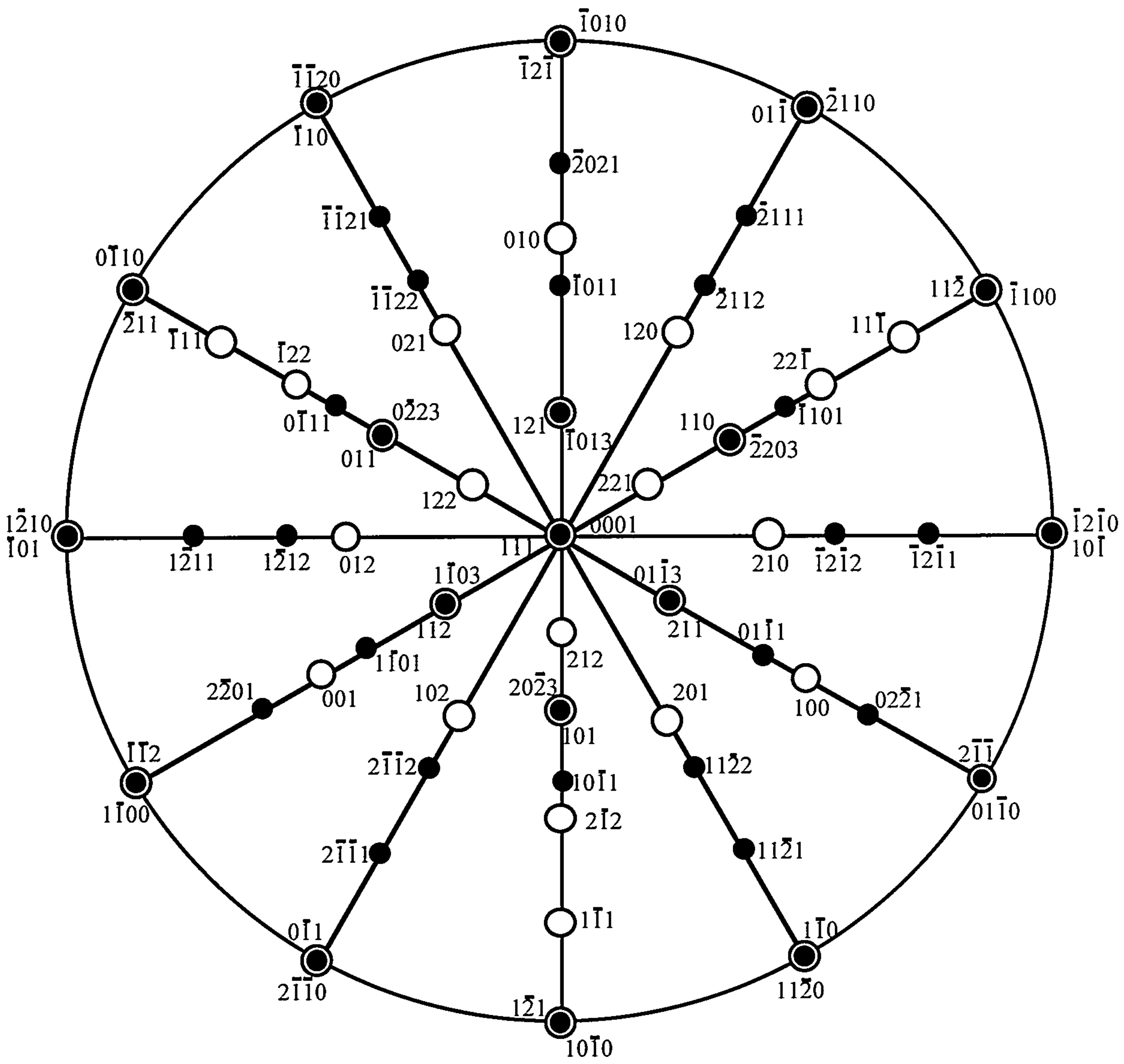

Figure 13. The composite stereogram for the C15 (○) and C14 (●) (*c*/*a*=1.631).

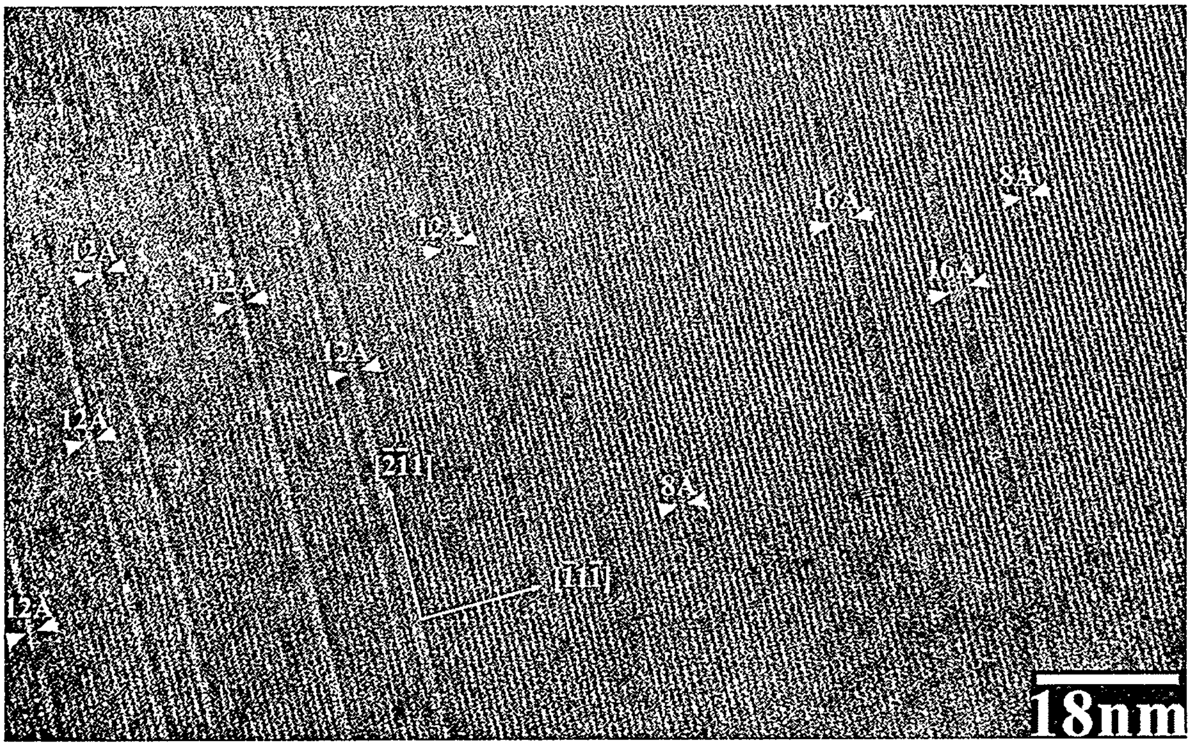

Figure 13. A high resolution image of heat treated powder shows C14 and C15 intercalation layers and C36 layer.

Mechanism

A similar prevalence of stacking faults on the close-packed layers formed by f.c.c.↔ h.c.p transformations have been found to occur in pure cobalt and cobalt based alloys such as CoNi and CoFe. Since the (111) planes in the f.c.c. phase and the basal planes (0001) in the h.c.p. phase have the same configuration of the atoms, Burgers [45] associated the fault structure with the hetergeneous shear of the transformation. This mechanism involves a lattice shear resulting from the glide of Shockley-type partial dislocations on the system $(111)[\bar{1}\bar{1}2]$. This motion shifts the entire crystal above the glide plane by the vector $\frac{1}{6}[\bar{1}\bar{1}2]$ and produces an intrinsic stacking fault in the f.c.c. structure, i.e. a h.c.p. layer. This shear only occurs on alternate planes and so converts the XYZ ... sequence of the (111) planes in the f.c.c. structure to the XY... sequence of basal planes in the h.c.p. structure.

Because the crystal relationship between the C14 and C15 structures is analogous to that between the f.c.c. and h.c.p., the ordinary shear mechanism can be used to explain the transition. However, the ordinary shear was claimed to occur with difficulty in Laves phases and a synchroshear mechanism was proposed by Hazzledine et al [42]. A synchroshockley partial dislocation consists of two ordinary Shockleys with different Burgers vectors gliding on two separate slip planes only 0.5 Å apart. According to this theory, the transformation of C14/C15 occurs if a synchroshockley glides through alternate triple layers.

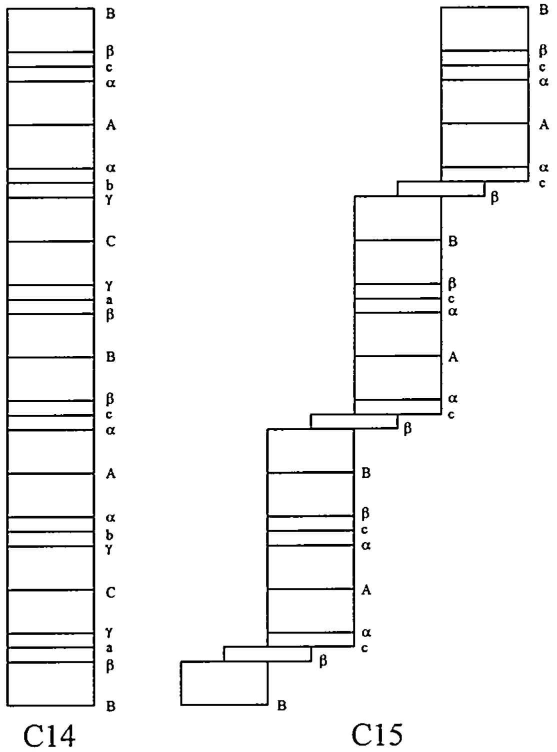

Figure 16. Schematic of the transition between the C15 and C14 can be achieved by synchroshear (indicated by steps) on every other triple layers (after [42]).

The transitions between the Laves phases are sluggish at room temperature. During the heat treatment, however, the synchroshockley glide become more mobile and the transition between the Laves phases becames considerable easier. In addition, vacancies introduced in Laves phases at high temperature may assist the movement of synchroshockley dislocations [46].

The formation of the faulted structure seen in the heat treated sample fits well with the synchroshockley glide mechanism. The conditions of increased number of vacancies and increased mobility at elevated temperature are both satisfied during heat treatment.

There might possibly be a diffusion component assisting the formation of the observed faults. TEM observations have shown that as the faulted structure develops during heat treatment, the interdendritic region is consumed. EDS studies also showed that the composition of the interdendritic region differs from that of the grain boundary particles. Thus, diffusion is clearly occurring. As the interdendritic region is consumed by grain growth, diffusion along the length of the faults might occur rapidly during heat treatment. This may result in slight shifts in composition in the region of faults that will affect the stability of the observed phase. More work needs to be done to determine exactly what occurs during heat treatment. However, as the following section shows, phase stability is affected by composition variations.

Phase Stability

For the C14 interdendritic phase, the axial ratio c/a is about 1.631, very close to the ideal value $\sqrt{8}/\sqrt{3} \approx 1.633$ according to the hard sphere model and within the range 1.63 and 1.65 as reported in the literature for the AB_2 type alloys with the C14 type structure [47].

The dendritic regions in the as-atomized powder are heavily faulted because the composition and the temperature is such that the C14 and C15 structures (and possibly other longer period structures) of the same composition of differing stacking arrangement have equal free energy.

In the HPGA process, the AB_2 type intermetallic alloy melt cooled into a region where the C14 and the C15 structures are equally stable with the structure susceptible to faulting. This was manifested by the appearance of a heavily faulted structure rather than discrete regions of C15 and C14 structures. Due to the rapid solidification, the structure was retained in the HPGA process. Upon subsequent heat treatment, the C15 structure primarily decomposes to the C14 structure, although it and the higher order C36 structure still exist as intercalation layers. The way in which the interdendritic phase is consumed suggests that this is accomplished by small changes in the chemical composition of the faulted grains.

The Laves phases are considered size compounds because the existence of a particular laves phase is governed by an atomic size relationship between the component elements. A r_A/r_B range of 1.05-1.67 is typically observed for Laves phases; outside this range, no Laves phases exists [48]. The essential factor appears to be that the ideal atomic radii ratio r_A/r_B of the participating atoms is 1.225 [49]. The atoms forming the phases tend to adjust in size to accommodate this ideal space-filling (1.225) in the Laves phase lattices. In this way a high packing density is achieved, which corresponding to an average coordination number of 13.3 [49] and a packing efficiency of 0.72 [50]. For the Laves-phase in the Zr-Ti-V-Ni system it was reported [51] that the C14 structure predominated when the ratio r_A/r_B was less than 1.225. For larger values the C15 predominated.

In this study, the atom size factor r_A/r_B was calculated and the results compared to the ideal atomic radii ratio to determine whether C14 or C15 should be favored. For these calculations, the Goldschmidt radius was used in order to be consistent with previous geometrical studies on the stability and appearance of Laves phases. The Goldschmidt radiis [52] of the elements in our materials are listed in Table 6.

Using the at% of Zr and Ti in the starting material for A and the nominal values of Ni, Mn, V and Cr for B radii for the system studied, the average Goldschmidt radius of A atoms and B atoms is:

$$r_A = \frac{\sum_{i=Zr,Ti} r_i \times (at.\%)_i}{\sum_{i=Zr,Ti} (at.\%)_i} = 1.50\text{Å}$$

$$r_B = \frac{\sum_{i=Ni,Mn,V,Cr} r_i \times (at.\%)_i}{\sum_{i=Ni,Mn,V,Cr} (at.\%)_i} = 1.23\text{Å}$$

Therefore, the atomic size ratio is: $r_A/r_B = 1.50/1.23 = 1.22$.

This result indicates that the composition of starting material is favorable to the Laves phase formation. However, since the value is so near the ideal 1.225, the C14 and C15 structures appear equally likely, assuming the alloy studied behaves similarly to the alloy of [51]. Thus, atomic radii ratio calculations alone can not be used to determine whether the C14 or C15 is the more stable structure.

When the atomic size factors are inconclusive, the electron concentration *e/a* has been identified as an important parameter in controlling the relative stability of the different Laves phase structures. The electron concentration *e/a* is defined as the average electron number per atom outside the closed shell of the component atoms.

The pioneer work of Laves and Witte [53, 54] on the effect of electron concentration on the stability of Laves phase alloys demonstrated that for several Mg-based systems alloy systems, the C15, C36 and C14 type Laves phase exist in order with increasing e/a. In their study the valence electron concentration was used to relate the crystal structure. Liu etc. [55, 56] have studied a number of binary Cr-X and Nb-X and ternary Nb- Cr-X alloys (the X denote transition-metal elements). They concluded that the average electron concentration e/a determines the phase stability of the $NbCr_2$-based transition-metal Laves phase. With e/a < 5.76, the C15 structure is stabilized while the C14 structure is stable with a e/a range of 5.88-7.53. The C15 will be stabilized again with e/a > 7.65. Further increasing electron concentration (e/a > 8) will result in the disordering of the alloy.

In this study, all elements that form the Laves Phases are transition metals. Therefore, for each element, the *e/a* ratio is simply the sum of the *s* electrons and *d* electrons outside its inert gas shell. The electron concentration of various transition elements used in the AB_2 type alloy of this study can be found in Table 6. We can calculate the average electron concentration for this material according to Liu's equation [55]:

$$(e/a)_{average} = \sum_i \left[(e/a)_i \times (at.\%)_i \right]$$

Using this equation for the as-atomized material, we obtain $(e/a)_{bulk}$=6.91. If we consider the dendritic and interdentritic regions separately, based on the composition as determined by EDS analysis, the electron concentration for these regions are: $(e/a)_{dendritic}$= 6.69, $(e/a)_{interdendritic}$ =7.05 respectively. If we accept Liu's conclusion that the C14 structure is stable with e/a range of 5.88-7.53, we can conclude once again that the C14 is the stable phase for both dendritic and interdendritic structures. The fact that C15 is seen in the HPGA powder indicates that the faulted structure of the dendritic region is metastable and exists due to the high solidification rate.

The average electron concentration is a simple and useful concept. According to the criteria, the change in the concentration of any element may result in a crystal structure change and a change in the stability between the C14 and C15 phases in the multiple phase alloys. Therefore, based on this concept, we can adjust the composition to obtain desired phases and materials performance.

Table 6. The Goldschmidt radius and the electron concentration of the elements.

Elements	Atomic No.	Goldschmidt Radius(Å)	Electronic Structure	e/a
Zr	40	1.60	Kr $4d^25s^2$	4
Ti	22	1.47	Ar $3d^24s^2$	4
Ni	28	1.25	Ar $3d^84s^2$	10
Mn	25	1.12	Ar $3d^54s^2$	7
V	23	1.36	Ar $3d^34s^2$	5
Cr	24	1.28	Ar $3d^54s^1$	6

Recommendations for Future Work

Some studies [57, 58] pointed out that C36 might exist as intermediate phases between the C14 and C15. Several stacking variants may exist in a narrow e/a range, confirming that small compositional changes can destabilize or stabilize the structures. However, no complete analysis has been given for this material. Faults that appear to be the C36 structure were found in this investigation. Additional studies are required in order to fully understand the role of this intermediate phase and its effect on the electrochemical performance. In addition, a further study on the powder with a prolonged heat treatment is needed to confirm the stability of the phases.

CONCLUSIONS

A proprietary and multicomponent AB_2 type alloy produced by HPGA were examined using XRD, SEM and TEM. The results can be summarized as follows:

First, the as-atomized powders possessed a dendritic growth microstructure. The dendrite consists of cubic C15 and hexagonal C14 structures and the arms are separated by an interdendritic region having the C14 structure. The C15 has lattice constant a=7.03Å and C14 has lattice constant a=4.97Å, c=8.11Å, which are consistent with Rietveld refinement analysis. The orientation relationship between the C14 and the C15 was determined to be $(111)[1\bar{1}0]_{C15}//(0001)[11\bar{2}0]_{C14}$. A polycrystalline region also exists in as-atomized powder, consisting of the C14 structure. This region is believed to be a chill zone on the surface of some powder that results from the rapid cooling.

Secondly, upon heat treatment the powder showed a change in appearance of the fault structure within the large grains. The grains appear to be equi-axed and the faults defined themselves into distinct layers of C1, C15 and possibly C36 structures within the grains. The interdendritic phase is consumed during heat treatment, leaving behind small particles rich in Zr and Ni scattering on the grain boundary. The region of fine grains changed to a mixture of C14 and C15 structures.

From these observations we can draw the following conclusions:

1. The orientation relationship between the C14 and the C15 was determined to be $(111)[1\bar{1}0]_{C15}//(0001)[11\bar{2}0]_{C14}$.
2. The C14 structure is the stable phase based on the discussion of the electron concentration.

3. The faulted structure of the dendritic regions in HPGA powder and in the heat treated grains is able to exist as discrete C14 and C15 layers due to the similarity of the C14 and C15 structures.
4. This implies that although C14 is stable phase, the remarkable similarity in crystal structures of various Laves phase types makes transitions from one to another fairly easy. Small composition fluctuations may affect the phase stability, causing the transition from one phase to the other to occur.

REFERENCES

1. A. F. Andresen and A. J. Maland, Hydrides for Energy Storage, Pergamon Press, New York, 1978.
2. D. Linden, Handbook of batteries, McGraw-Hill Inc., New York, 1995.
3. W.M. Muller, J.P. Blackledge and G.G. Libowitz, Metal Hydrides, Academic Press, New York, 1968.
4. C. Iwakura, M. Matsuoka and Kidorui, Rare Earths 17, 1990, p. 11.
5. M. Kopczyk and G. Wójcik, in New Promising Electrochemical Systems for Rechargeable Batteries, edited by V. Barsukov and F. Beck, NATO ASI Series, 1995, p. 265.
6. A. Anani, A. Visintin, K. Petrov, S. Srinivasan, J.J. Reilly, J.R. Johnson, R.B. Schwarz, and P.B. Desch, J. Power Sources 47, 1994, p. 261.
7. C. Iwakura and M. Matsuoka, Progress in Batteries & Battery Materials 10, 1991, p. 81.
8. J. J. Reilly, in Proc. Symp. Hydrogen Storage Materials, Batteries and Electrochemistry, 92-5, edited by D.A. Corrigan and S. Srinivasan, The Electrochemical Society, Pennington, NJ, 1992, p. 24.
9. H. H. Van Mal, K.H. J. Buschow and A. R. Miedema, J. Less-Comm Met. 35, 1974, p. 65.
10. Y. Huang, W. Liu and D. Zhu, in New Promising Electrochemical Systems for Rechargeable Batteries, edited by V. Barsukov and F. Beck, NATO ASI Series, 1995, p. 249.

11. S. Venkatesan, M.A. Fetcenko, D.A. corrigan, P.R. Gifford, S.K. Dhar and S.R. Ovshinsky in Materials for Electrochemical Energy Storage and Conversion-Batteries, Capacitors and Fuel Cells, edited by D. H. Doughty, B. Vyas, T. Takamura and J. R. Huff, Mat. Res. Soc. Symp. Proc. 393, 1995, p. 243.
12. M.A. Fetcenko, S. Venkatesan and S.R. Ovshinsky, in Proc. Symp. Hydrogen storage Materials, Batteries and Electrochemistry, 92-5, Edited by D.A. corrigan and S. Srinivasan, The Electrochemical Society, Pennington, NJ, 1992, p. 76.
13. S. R. Ovshinsky and M.A. Fetcenko and J. Ross, Science 260, 1993, p. 176.
14. R. B. Schwarz, R.R. Petrich and C.K. Saw, J. Non-Cryst. Solids 76, 1985, p. 281.
15. M. Jurczyk, W. Rajewski, G. Wójcik, and W. Majchrzycki, J. Alloy and Compounds 278, 1999, p. 250.
16. M. Jurczyk, W. Rajewski, G. Wójcik, and W. Majchrzycki, J. Alloy and Compounds 274, 1998, p. 299.
17. M.A. Fetcenko, S. Venkatesan and S.R. Ovshinsky in Proc. Symp. Hydrogen Storage Materials, Batteries and Electrochemistry Vol. 92-5, edited by D. A. Corrigan and S. Srinivasan, The Electrochemical Society, Pennington, NJ, 1992, p. 141.
18. M. A. Fetcenko, S. Sumner and J. LaRocca, US Patent No. 4.948.423, 1989.
19. N. Cui and J.L. Luo, International Journal of Hydrogen Energy 24, 1999, p. 37.
20. G. Wójcik and M. Kopczyk in New Promising Electrochemical Systems for Rechargeable Batteries, edited by V. Barsukov and F. Beck, NATO ASI Series, 1995, p. 276.
21. S.R. Ovshinsky and M.A. Fetcenko, U.S. Patent No. 5 277 999, 1994.

22. T. Sakai, M. Matsuoka and C. Iwakura, in Handbook on the Physics and Chemistry of Rare Earths, edited by K.A. Gschneider, Jr. and L. Eyring, Elsevier Science, New York, 21, 1995, p.133.

23. T. B. Massalski, in Physical Metallurgy Part 1, edited by R. W. Cahn and P. Hassen, North-Holland, New York, 1983, p. 190.

24. A. G. Jackson, Handbook of Crystallography for Electron Microscopists and Others, Springer-Verlag, New York, 1991.

25. F. Laves, Intermetallic Compounds, edited by J.H. Westbrook, J. Wiley, New York 1967.

26. N. Miyamura, T. Sakai, N. Kuriyama, K. Oguro, A. Kato and M. Ishikawa, in Proc. Symp. Hydrogen Storage Materials, Batteries and Electrochemistry, 92-5, edited by D.A. Corrigan and S. Srinivasan, The Electrochemical Society, Pennington , NJ, 1992, p. 179.

27. V. Pecharsky (private communication).

28. L.C. Daams, P. Villars, and JHN van Vucht, Atlas of crystal structure types for intermetallic phases, ASM International, Materials Park, OH, 1991.

29. A. Anani, A. Visintin, S. Srinivasan and A. J. Appleby, in Proc. Sympo. Hydrogen Storage Materials, Batteries and Electrochemistry, 92-5, eidted by D. A. Corrigan and S. Srinivasan, The Electrochemical Society, Pennington, NJ, 1992, p. 105.

30. A. Anani, A. Visintin, S. Srinivasan and A. J. Appleby, Ext. Abstr. 183rd Meet. Electrochemical Society, 93-1, The Electrochemical Society, Princeton, NJ, 1993, p. 82.

31. A. Anani, K. Petrov, S. Srinivasan, A. J. Appleby, J. J. Reilly, J.R. Johnson and H. S. Lim, Ext. Abstr. 183rd Meet. Electrochemical Society, 93-1, The Electrochemical Society, Princeton, NJ, USA, 1993, p. 79.

32. J. Yu, B. Liu, K. Cho and J. Lee, J. Alloy and Comp 278, 1998, p. 283.
33. M. Yoshida and E Akida, J. Alloys Comp. 224, 1995, p. 121.
34. J. Huot, E. Akiba and H. Iba, J. Alloys Comp. 228, 1995, p. 181.
35. J. Huot, E. Akiba and Y. Ishido, J. Alloys Comp. 231, 1995, p. 85.
36. H. H. Lee, K. Y. Lee and J. Y. Lee, J. Alloys Comp. 253-254, 1997, p. 601.
37. X. G. Yang, Y. Q. Lei, W. K. Zhang, G. M. Zhu and Q. D. Wang, J. Alloys and Comp. 243, 1996, p. 151.
38. G. Cliff and G. Lorimer, Proc. 5th European Cong. on Electron Microscopy, 1972, p. 140.
39. A. Suzuki, N. Nishimiya, Materials Research Bulletin 19, 1984, p. 1559.
40. I. Anderson and V. Pecharsky (private communication).
41. M. Sluiter and P. E. A. Turchi, Phy. Rev. B 43, 1991, 12251.
42. P. M. Hazzledine, K. S. Kumar, D. B. Miracle and A.G. Jackson, Mat. Res. Soc. Symp. Proc. 288, 1993, p. 591.
43. K. S. Kumar and P. M. Hazzledine, Mat. Res. Soc. Symp. Proc. 288, 1993, p. 1383.
44. X. Y. Song, X. B. Zhang, Y. Q. Lei, Z. Zhang and Q. D. Wang, International Journal of hydrogen Energy 24, 1999, p. 455.
45. W. G. Burgers, Physica I, 1934, p. 561.
46. P. M. Hazzledine and P. Pirouz, Scripta Metall. Mater. 28, 1993, p. 1277.
47. Y. Moriwaski, T. Gamo and T. Iwaki, J. Less-Common Met 172-174, 1991, p. 1028.
48. M. V. Nevitt, in Electron structure and alloy chemistry of the transition elements, edited by P.A. Beck, Interscience Publishers, New York, 1963, p. 101.

49. P. Haasen, Physical Metallurgy, Cambridge University Press, Cambridge, UK, 1996, p. 143.

50. D. J. Thoma and J. H. Perepezko, J. Alloys and Comp. 224, 1995, p. 330.

51. H. Nakano, I. Wada and S. Wakao, J. Adv. Sci. 4, 1992, p. 239.

52. Goodfellow Catalog: Metals, alloys, compounds ceramics, polymers, composites 1995/1996, Goodfellow Corporation, 800 Lancaster Avenue, Berwyn, PA.

53. F. Laves and H. Witte, Metallwirschaft 14, 1935, p. 645.

54. F. Laves and H. Witte, Metallwirschaft 15, 1936, p. 840.

55. J. H. Zhu, P. K. Liaw and C. T. Liu, Mater. Sci. Engr. A239-240, 1997, p. 260.

56. J. H. Zhu, C. T. liu and P. K. Liaw, Intermetallics 7, 1999, p. 1011.

57. D. J. Thoma and J. H. Perepezko, Mater. Sci. Eng. A 156, 1992, p. 97.

58. S. Hong and C. L. Fu, Intermetallics 7, 1999, p. 5.

ACKNOWLEDGEMENTS

This work was performed at Ames Laboratory under Contract No. W-7405-Eng-82 with the U.S. Department of Energy. The United States government has assigned the DOE Report number IS-T 1871 to this thesis.

I would like to thank the Program of Study Committee who helped plan and directed this study: Professors Scott Chumbley, Iver Anderson and Kurt Hebert. Special thanks to my major professor Scott Chumbley for his guidance and encouragement in learning TEM, which I deem an extremely useful instrument. Although I have been working on it for nearly two years, there is still much to learn and fully utilize its unique capabilities.

I also gratefully acknowledge the help of Vitalij Pecharsky and Fran Laabs of the Ames Laboratory in sample preparation and result interpretations.